

## Termination-dependent surface properties in the giant-Rashba semiconductors $\text{BiTeX}$ ( $X = \text{Cl}, \text{Br}, \text{I}$ )

Sebastian Fiedler,<sup>1</sup> Thomas Bathon,<sup>2</sup> Sergey V. Eremeev,<sup>3,4,5</sup> Oleg E. Tereshchenko,<sup>5,6,7</sup> Konstantin A. Kokh,<sup>5,7,8</sup> Evgueni V. Chulkov,<sup>4,5,9,10</sup> Paolo Sessi,<sup>2</sup> Hendrik Bentmann,<sup>1,\*</sup> Matthias Bode,<sup>2</sup> and Friedrich Reinert<sup>1</sup>

<sup>1</sup>*Experimentelle Physik VII and Röntgen Research Center for Complex Materials (RCCM), Universität Würzburg, Am Hubland, D-97074 Würzburg, Germany*

<sup>2</sup>*Experimentelle Physik II and Röntgen Research Center for Complex Materials (RCCM), Universität Würzburg, Am Hubland, D-97074 Würzburg, Germany*

<sup>3</sup>*Institute of Strength Physics and Materials Science, 634055 Tomsk, Russia*

<sup>4</sup>*Tomsk State University, 634050 Tomsk, Russia*

<sup>5</sup>*Saint Petersburg State University, 198504 Saint Petersburg, Russia*

<sup>6</sup>*Institute of Semiconductor Physics, 636090 Novosibirsk, Russia*

<sup>7</sup>*Novosibirsk State University, 636090 Novosibirsk, Russia*

<sup>8</sup>*Institute of Geology and Mineralogy, SB RAS, 630090 Novosibirsk, Russia*

<sup>9</sup>*Donostia International Physics Center (DIPC), 20018 San Sebastián/Donostia, Basque Country, Spain*

<sup>10</sup>*Departamento de Física de Materiales and Centro Mixto CSIC-UPV/EHU, Facultad de Ciencias Químicas, Universidad del País Vasco/Euskal Herriko Unibertsitatea, Apartado 1072, 20080 San Sebastián/Donostia, Basque Country, Spain*

(Received 12 October 2015; published 15 December 2015)

The noncentrosymmetric semiconductors  $\text{BiTeX}$  ( $X = \text{Cl}, \text{Br}, \text{I}$ ) show large Rashba-type spin-orbit splittings in their electronic structure making them candidate materials for spin-based electronics. However,  $\text{BiTeI}(0001)$  single-crystal surfaces usually consist of stacking-fault-induced domains of Te and I terminations implying a spatially inhomogeneous electronic structure. Here we combine scanning tunneling microscopy, photoelectron spectroscopy (ARPES, XPS), and density functional theory calculations to systematically investigate the structural and electronic properties of  $\text{BiTeX}(0001)$  surfaces. For  $X = \text{Cl}, \text{Br}$  we observe macroscopic single-terminated surfaces. We discuss chemical characteristics among the three materials in terms of bonding character, surface electronic structure, and surface morphology.

DOI: [10.1103/PhysRevB.92.235430](https://doi.org/10.1103/PhysRevB.92.235430)

PACS number(s): 71.70.Ej, 68.37.Ef, 79.60.-i, 71.22.+i

### I. INTRODUCTION

The narrow-gap semiconductors  $\text{BiTeX}$  ( $X = \text{Cl}, \text{Br}, \text{I}$ ) have attracted considerable interest because of large Rashba-type spin-orbit splittings in their bulk and surface electronic structures [1–3], which have been observed by angle-resolved photoelectron spectroscopy (ARPES) [4–8] and magnetotransport measurements [9,10]. The enhanced spin splitting in these materials is driven by their noncentrosymmetric crystal structure in combination with strong atomic spin-orbit coupling and a negative crystal-field splitting of the topmost valence bands [11]. The latter features have also been predicted to promote a topological insulator phase in  $\text{BiTeI}$  under application of external pressure [12]. The  $\text{BiTeX}$  series does not only host the presently largest known Rashba effect of all semiconductors; it also appears more suitable for possible spin-electronic applications [13,14] than artificially grown monolayer reconstructions, such as metallic surface alloys, where spin splittings of similar magnitude can be achieved [15–18].

At the surface, the noncentrosymmetric, layered unit cell of  $\text{BiTeX}$  results in two possible polar terminations [4,6,8,19], Te- and X-terminated surfaces, that give rise to n-type or p-type band bending, respectively [4]. The surface properties may be influenced additionally by defects, as is the case for  $\text{BiTeI}$ , where bulk stacking faults induce coexisting Te- and

I-terminated domains on microscopic length scales as shown by scanning tunneling microscopy (STM) [20–23]. While the resulting lateral interfaces between surface areas of different terminations may provide interesting new physics [20,21], the presence of multiple domains will in most instances be undesirable. For  $\text{BiTeCl}$  and  $\text{BiTeBr}$  spatially resolved surface investigations have so far been scarce [24]. In the case of  $\text{BiTeCl}$  photoemission experiments indicate single-terminated surfaces [6], in contrast to  $\text{BiTeI}$ , whereas for  $\text{BiTeBr}$  the situation is unclear. The majority of ARPES studies of  $\text{BiTeX}$  point to similar Rashba-split band structures for all three compounds [6–8,25], in agreement with theoretical predictions [2,8]. However, for  $\text{BiTeCl}$  the existence of topological surface states has also been claimed based on ARPES [26] and STM [24].

In this work we present a combined investigation of the surface structural and electronic properties of the  $\text{BiTeX}$  semiconductors. Our STM experiments show that  $\text{BiTeBr}$  and  $\text{BiTeCl}(0001)$  display single-domain surfaces with X- or Te-termination. The determined terrace step heights agree with the respective bulk unit cell parameters, and x-ray photoemission (XPS) provides depth-dependent chemical information in line with the expected layered atomic structure. The measured core level binding energies indicate a significant charge transfer from Bi to both X and Te in agreement with density functional theory (DFT) calculations. We systematically compare the electronic properties of Te- and X-terminated surfaces in terms of band bending, surface band structure, work function, atomic defects, and reaction to deposited adsorbate atoms.

\*hendrik.bentmann@physik.uni-wuerzburg.de

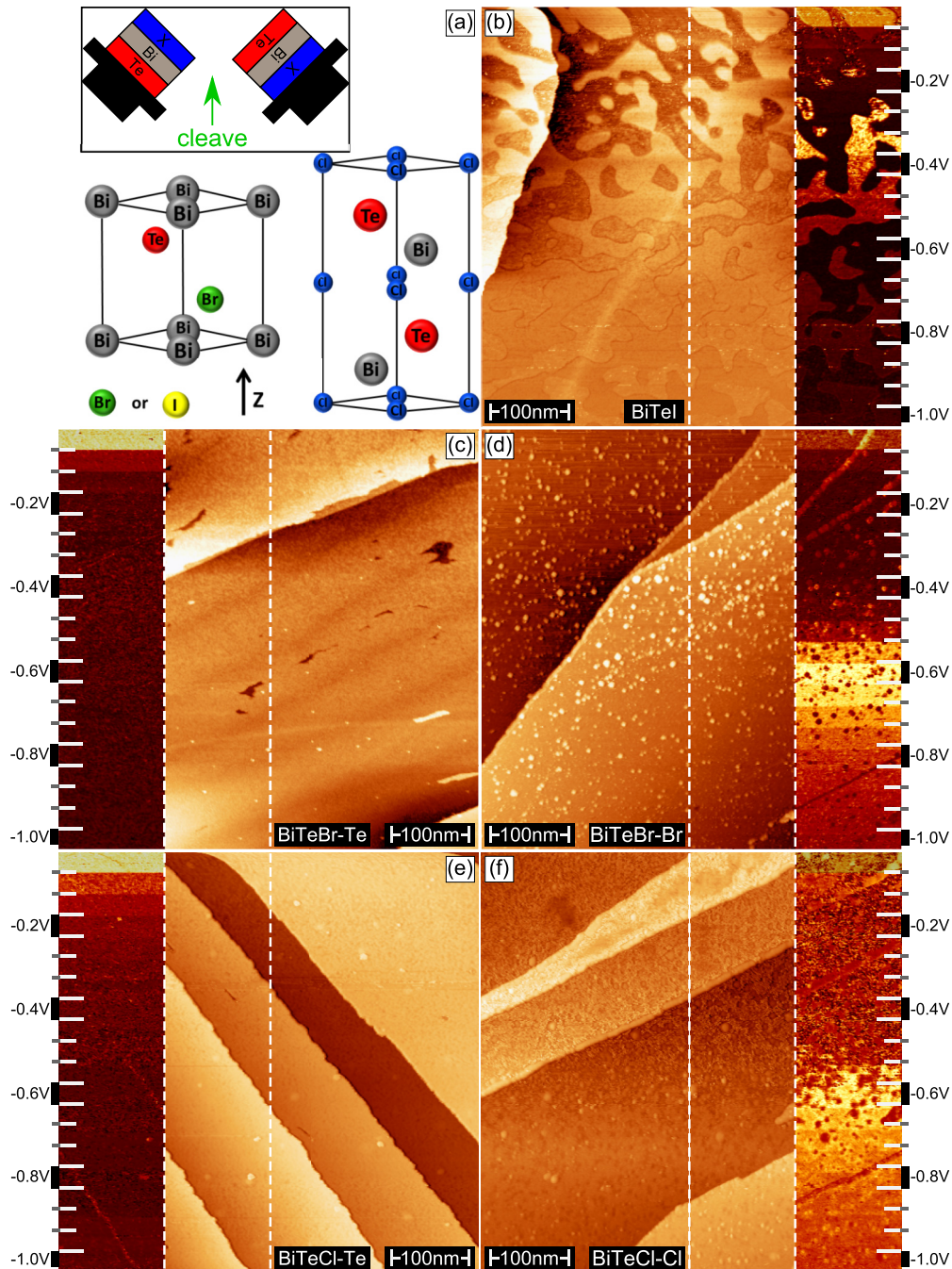


FIG. 1. (Color online) Crystal structure and room-temperature STM measurements for  $\text{BiTeX}$ . (a) Bulk unit cells of  $\text{BiTeBr/I}$  and  $\text{BiTeCl}$  and the resulting surface terminations after cleaving. The inset sketches the situation for an ideal crystal mounted between the two sample holders (black) after the cleave. STM measurements ( $500 \text{ nm} \times 500 \text{ nm}$ ) of (b)  $\text{BiTeI}$ , (c) Te-terminated and (d) Br-terminated  $\text{BiTeBr}$ , as well as (e) Te-terminated and (f) Cl-terminated  $\text{BiTeCl}$ . The gap voltage is varied from  $-0.05 \text{ V}$  to  $-1 \text{ V}$  and the tunneling current was  $0.1 \text{ nA}$  in (b) and  $0.2 \text{ nA}$  in (c)–(f). The outermost parts of the images are  $dI/dV$  maps of the areas between the lines.

## II. METHODS

Our experimental setup is designed for a comprehensive analysis of the geometric and electronic properties in real and reciprocal space as described in Ref. [23]. The system allows surface analytics by means of various techniques, i.e., LEED, SPA-LEED, STM, STS, AFM, XPS, work function, and ARPES measurements in ultrahigh-vacuum conditions for the same sample without exposing it to air. Additional high-

resolution STM measurements were performed at a separate setup with a low-temperature STM (Omicron LT-STM) at  $T = 5 \text{ K}$ .

We used a modified sample holder system, which allowed us to split single crystals *in situ* and to measure both corresponding surfaces of a cleave without the need to reglue or to expose the sample to air [see Fig. 1(a)]. Thus,  $\text{BiTeX}$  ( $X = \text{Cl, Br, I}$ ) single crystals were cleaved at room temperature along the (0001) direction at low pressures  $2 \times 10^{-10} \text{ mbar}$  revealing

surfaces of about  $2\text{ mm} \times 2\text{ mm}$  on each side. A podium smaller than the sample was used to move the surface into the focal point of the electron spectrometer in order to minimize spurious signal from the sample holder.

Submonolayer amounts of Cs were deposited using commercial alkali dispensers (SAES Getters). All experiments were performed at room temperature except for those carried out at the LT-STM.

Tips have been prepared according to Ref. [23]. Differential conductance maps are used to obtain spatially resolved information about the sample's local density of states (DOS). For this purpose a small modulation voltage ( $U_{\text{mod}} = 25\text{ mV}$ ) is added to the sample bias  $V$  and the resulting variation of the tunneling current,  $dI/dV$ , is recorded simultaneously with the topographic, i.e., constant-current, image. STM data were processed with the WSxM software package [27].

XPS measurements were done with Al  $K\alpha$  radiation ( $h\nu = 1486.6\text{ eV}$ ) under a photoelectron emission angle of  $60^\circ$  in order to enhance the surface sensitivity of the experiment. The x-ray source was not monochromatized and the spectra were satellite corrected. The energy resolution of the XPS measurements was about  $1\text{ eV}$ . ARPES data were acquired with a nonmonochromatized He discharge lamp with He  $I\alpha$  radiation ( $h\nu = 21.2\text{ eV}$ ) and at an energy resolution of approximately  $25\text{ meV}$ . Work functions were determined from the secondary photoelectron cutoff with the sample held on a positive potential of  $9\text{ V}$ . Calibration measurements for Au(111) gave values in line with previous reports [28,29].

The synthesis of the charges was performed by fusing binary compounds:  $\text{Bi}_2\text{Te}_3$  with  $\text{BiCl}_3$ ,  $\text{BiBr}_3$  and  $\text{BiI}_3$ , correspondingly. According to published data [30,31]  $\text{BiTeI}$  and  $\text{BiTeBr}$  melt congruently at  $560^\circ\text{C}$  and  $526^\circ\text{C}$ , while  $\text{BiTeCl}$  shows incongruent melting [31] at  $430^\circ\text{C}$  with a peritectic composition around  $11\text{ mol.}\% \text{Bi}_2\text{Te}_3 + 89\text{ mol.}\% \text{BiCl}_3$ . Therefore we have used stoichiometric charge for  $\text{BiTeI}$ ,  $\text{BiTeBr}$ , and melt-solution system with a molar ratio  $\text{Bi}_2\text{Te}_3 : \text{BiCl}_3 = 1 : 9$  for the crystallization of  $\text{BiTeCl}$ . The synthesis was performed directly in the growth quartz ampoules at a temperature which is  $20^\circ\text{C}$  above the melting point. Crystal growth was performed by the modified Bridgman method with rotating heat field [32]. After pulling the ampoules through the vertical temperature gradient of  $15^\circ\text{C}/\text{cm}$  at  $10\text{ mm}/\text{day}$ , the furnace was switched off.

Complementary first-principles calculations were performed within the framework of the density functional theory (DFT) using the projector-augmented-wave (PAW) [33,34] basis. The generalized gradient approximation (GGA-PBE) [35] to the exchange correlation (XC) potential as implemented in the VASP code [36,37] was used. The relaxed bulk parameters have been taken into account. The atomic charges were estimated by implementing the Bader charge analysis [38].

### III. RESULTS

#### A. Surface morphology and bonding character

Figure 1(a) shows the unit cells of  $\text{BiTeX}$ . While  $\text{BiTeI}$  and  $\text{BiTeBr}$  have a unit cell of 3 atomic layers, the one of  $\text{BiTeCl}$  comprises 6 layers along  $z$  resulting in a height twice as large [2,39]. The inset sketches the stacking order after the cleave of

an ideal single crystal, resulting in two different terminations for the two opposing surfaces.

Figure 1(b) displays a  $500\text{ nm} \times 500\text{ nm}$  STM measurement of  $\text{BiTeI}(0001)$  at  $0.1\text{ nA}$  tunneling current. During the scan the gap voltage was gradually decreased from  $-0.05\text{ V}$  at the upper part of the image down to  $-1.0\text{ V}$  at the lower part. Note that negative voltages refer to tunneling from the sample to the tip, thus reflecting the occupied DOS of the sample as being also accessed by ARPES spectra. Coexisting Te- and I-terminations are visible as reported earlier [20–23]. The outer part of the image shows the corresponding  $dI/dV$  map of the surface within the two white dashed lines. The Te-terminated surface shows a high DOS at  $-0.05\text{ V}$  while at  $-0.3\text{ V}$  the same surface appears dark in the  $dI/dV$  map and the I-terminated surface reveals a high intensity. This high DOS originates from the onsets of the band structures of the two different terminations, as shown in Ref. [23]. The step edges within the same terminations are around  $0.7\text{ nm}$  high and the ratio between Te- to I-terminated areas is roughly 50/50.

Next we investigate the surface morphologies of  $\text{BiTeBr}$  and  $\text{BiTeCl}$  [see Figs. 1(c)–1(f)]. The images reflect a surface area of  $500\text{ nm} \times 500\text{ nm}$ , and were obtained at  $0.2\text{ nA}$  tunneling current at a voltage varied from  $-0.05\text{ V}$  to  $-1\text{ V}$ . The surface terminations are indicated in the figures by  $\text{BiTeBr-Te}$  and  $\text{BiTeBr-Br}$  for the Te- and Br-terminated surfaces of  $\text{BiTeBr}$  and by  $\text{BiTeCl-Te}$  and  $\text{BiTeCl-Cl}$  for the Te- and Cl-terminated surfaces of  $\text{BiTeCl}$ , respectively.

Figure 1(c) shows one side of a  $\text{BiTeBr}$  crystal split at the (0001) direction. On this surface there is no sign of a second termination as seen in Fig. 1(b) for  $\text{BiTeI}$ . The step edges are  $(0.65 \pm 0.05)\text{ nm}$  high, which is in agreement with the bulk unit cell height along  $z$  [39]. Some adsorbates can be seen but the surface is mostly clean. An increase in the DOS close to  $E_F$  indicates that we are dealing with the Te termination of  $\text{BiTeBr}$ , as has been shown for  $\text{BiTeI}$  in Fig. 1(b) and Ref. [23].  $dI/dV$  maps taken over a larger energy range (not shown) further showed an onset of valence states at an energy of approximately  $-1\text{ eV}$ . Figure 1(d) shows the other side of the cleave. More adsorbates can be found on this surface, which indicates a higher chemical reactivity. The  $dI/dV$  map strongly deviates from the one obtained for the Te termination. At a gap voltage of around  $-0.55\text{ eV}$  an increase in the DOS can be seen, indicating a band onset, as observed similarly for the I termination of  $\text{BiTeI}$  in Fig. 1(b). Furthermore, the adsorbates appear dark in the  $dI/dV$  and start accumulating at the step edges before covering the terraces. The higher chemical reactivity and the determined DOS indicate that this surface is Br terminated. For  $\text{BiTeCl}$  similar observations in terms of DOS and adsorbate characteristics are obtained as for  $\text{BiTeBr}$ . The STM images and  $dI/dV$  maps for the Te- and Cl-terminated surface are shown Figs. 1(e) and 1(f), respectively, closely resembling their counterparts in  $\text{BiTeBr}$ . Notably, most of the step edges have a height of  $(1.25 \pm 0.05)\text{ nm}$  for both terminations, matching again the height of the bulk unit cell [39], while only 5%–10% of the steps have a height of  $\approx 0.7\text{ nm}$ , corresponding to a single  $\text{BiTeCl}$  trilayer.

Our STM measurements thus reveal strikingly different surface morphologies for  $\text{BiTeBr}$  and  $\text{BiTeCl}$  as compared to  $\text{BiTeI}$ . Both compounds feature single-domain (0001) surfaces

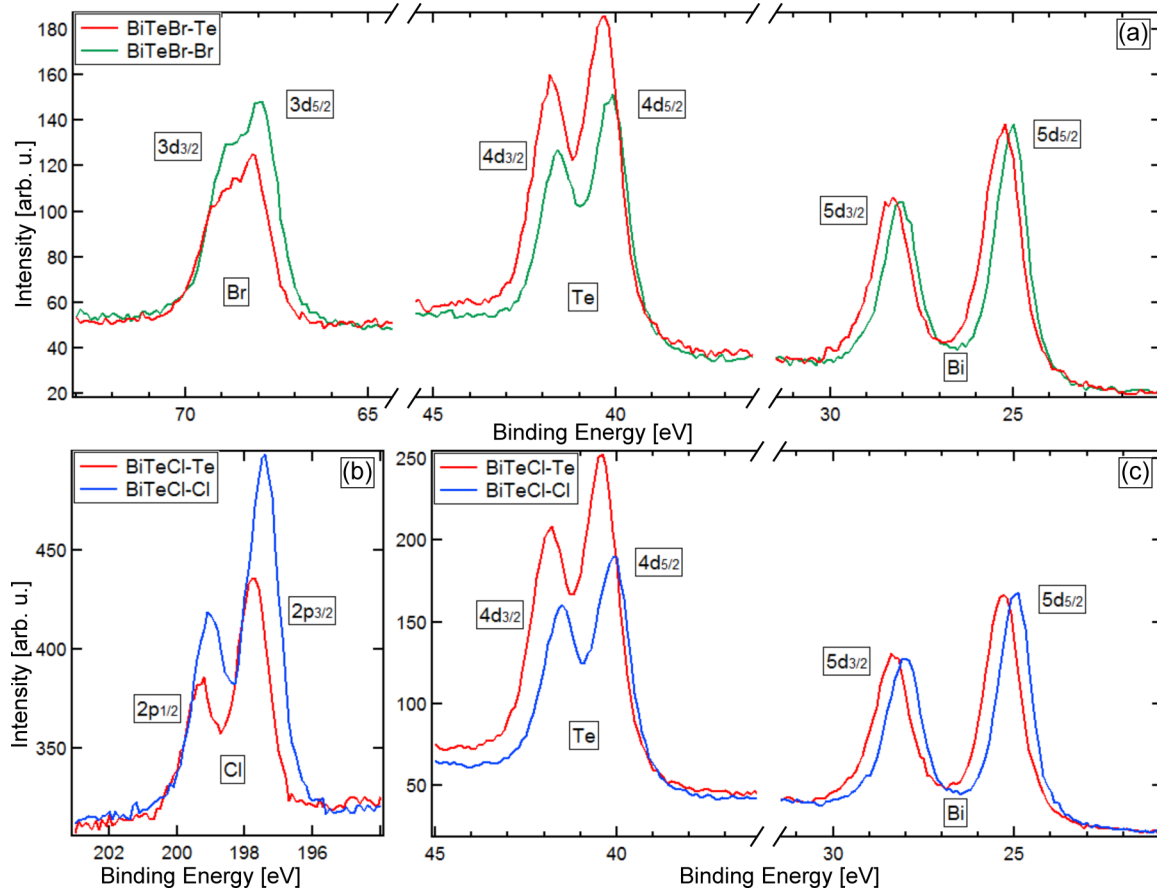


FIG. 2. (Color online) X-ray photoemission data for BiTeBr in (a) and BiTeCl in (b), (c). Characteristic intensity differences in the Te and Br/Cl core level signals are observed for the different surface terminations, reflecting the changed atomic stacking orders and the finite probing depth of the experiment. Furthermore, band bending gives rise to small energy shifts between the spectra for Te-terminated and Br/Cl-terminated surfaces.

with either Te- or X-termination. Apparently, bulk stacking faults, giving rise to domains of different stacking order in BiTeI, are largely absent in the other two compounds. A possible explanation for this behavior could be the similar atomic radii of Te and I atoms, that might be expected to promote the formation of mixed Te/I layers during the crystal growth. Our DFT calculations indicate that the formation energy for stacking faults in the bulk is much smaller for BiTeI (1 meV) than for BiTeBr (46 meV) and BiTeCl (60 meV), in line with the experimental findings. In general, BiTeBr and BiTeCl will thus be more suitable materials for spatially averaging techniques that address the spin polarization of the electronic bulk states.

To gain further insight into the structural and chemical properties of the BiTeBr and BiTeCl(0001) surfaces we have performed XPS experiments. Figures 2(a)–2(c) show core level spectra directly corresponding to the different surfaces presented in Fig. 1. Comparing spectra for Te- and Br(Cl)-terminated surfaces we observe a relative shift of 200 meV (300 meV), which we attribute to band bending [4,6,8]. The energy shifts are slightly reduced compared to values reported in Ref. [8], which might be due to the higher excitation energy and thus an increased probing depth in the present experiments.

Considering the peak intensities for the Te and Br(Cl) species we observe characteristic differences between two

surfaces with different termination resulting from the finite electron mean free path of the XPS experiment of around 1 nm [40]. When going from Te- to X-terminated surfaces the Te signal is reduced while the X signal is enhanced, directly reflecting the changed atomic stacking sequence. The spectra have been normalized to the signal of Bi which for both terminations is expected to reside in the second atomic layer as shown in the inset of Fig. 1(a). For a quantitative estimation we assume an exponential damping of the signal which amounts to roughly 30% for two atomic layers and the present experimental conditions [40]. From the data in Fig. 2(a) we infer that the Te 4d and Br 3d signals change by 22% and 25%, respectively. In Figs. 2(b) and 2(c) the change for the Te 4d core level is 30% and 36% for Cl 2p. Averaged over four samples, the damping for BiTeBr is  $26\% \pm 5\%$  for Te- and  $19\% \pm 6\%$  for Br-terminations while for BiTeCl we find  $32\% \pm 3\%$  for Te- and  $24\% \pm 13\%$  for Cl-terminated surfaces. The XPS data thus confirm the single termination and the expected termination-dependent atomic layer stacking for BiTeBr and BiTeCl.

Table I summarizes the binding energies for the Te  $4d_{5/2}$  and Bi  $5d_{5/2}$  peaks in BiTeX, which contain information about the chemical bonding in the compounds [40]. The aforementioned band bending gives rise to small deviations between different terminations on the order of 200–300 meV. Furthermore,

TABLE I. Core level binding energies and work functions for  $\text{BiTeX}$  and  $\text{Bi}_2\text{Te}_3$ . The estimated uncertainty of the measured values amounts to  $\pm 0.1$  eV. For comparison we also show the corresponding binding energies for elemental Bi and Te metal taken from Ref. [41].

	elem. (eV)	$\text{Bi}_2\text{Te}_3$ (eV)	Cl (eV)	$\text{TeCl}$ (eV)	Br (eV)	$\text{TeBr}$ (eV)	$\text{BiTeI}$ (eV)
Bi $5d_{5/2}$	24.1	24.6	25.0	25.3	25.0	25.2	25.0
Te $4d_{5/2}$	40.5	39.9	40.1	40.4	40.1	40.3	40.1
work function		5.1	6.2	4.5	6.0	4.7	(5.2)

when compared to the values in Bi and Te metal [41], the Bi  $5d_{5/2}$  peaks are shifted to higher and the Te  $4d_{5/2}$  peaks to lower binding energies. The absolute shift is significantly larger for Bi than for Te. On the other hand, no clear trends along the series  $X = \text{Cl, Br, I}$  are apparent. To gain a better understanding of the experimental data we have calculated by use of DFT the charge transfer in bulk  $\text{BiTeX}$  as shown in Table II. As one can see, the Bi atom loses about one electron by transferring it to Te ( $\sim 0.4e$ ) and  $X$  atoms which is in line with the experimental result. Note that among the three compounds the values for Bi vary by only 10%–20% and are basically the same for Te. This might explain the absence of clear chemical trends in the respective XPS binding energies. The considerable increase in the calculated charge transfer to  $X$  along  $X = \text{I, Br, Cl}$  further indicates an increasingly ionic bonding character between  $X^-$  and  $\text{BiTe}^+$  layer with rising electronegativity of the halogen atoms.

Additional insight into the influence of the halogen species on the bonding character may be gained by a comparison to  $\text{Bi}_2\text{Te}_3$ , showing a similarly layered structure as  $\text{BiTeX}$ , where a single Bi layer resides between two Te layers (see, e.g., Ref. [42]). For this compound the chemical shift of the Bi  $5d_{5/2}$  line is considerably reduced (see Table I). This points to significant differences between  $\text{BiTeX}$  and  $\text{Bi}_2\text{Te}_3$ , for which the bonding is usually assumed to be dominated by covalent contributions [43].

Table I also displays work functions for  $\text{BiTeX}$  as determined by the secondary photoelectron cutoff. For  $X = \text{Cl, Br}$  large differences above 1 eV between  $X^-$  and Te-terminated surfaces are observed in quantitative agreement with a recent STM study of the local work function on  $\text{BiTeI}(0001)$  [22]. This finding may indeed be understood in terms of an ionic bonding between  $X^-$  and  $\text{BiTe}^+$  layers creating opposite dipoles near the surface depending on termination [1,4,8,19–21,39]. Furthermore, the larger calculated charge transfer in  $\text{BiTeCl}$  compared to  $\text{BiTeBr}$  is in line with the increased work function difference between the two terminations observed experimentally. The work function for a  $\text{Bi}_2\text{Te}_3(0001)$  surface, which is terminated by a Te layer [42], is considerably larger than for the Te-terminated  $\text{BiTeBr}$  and  $\text{BiTeCl}$  surfaces, again pointing to a strong effect of the halogen atoms on the

TABLE II. Calculated charge transfer based on DFT in the bulk  $\text{BiTeX}$  compounds (in electrons).

	$\text{BiTeCl}$	$\text{BiTeBr}$	$\text{BiTeI}$
Bi	−1.09	−1.01	−0.91
Te	+0.41	+0.42	+0.44
$X$	+0.68	+0.59	+0.47

microscopic charge distribution. Surprisingly, for  $\text{BiTeI}$  only one cutoff could be observed in our spectra despite the presence of Te- and I-terminated surface areas. The Te and I domains of  $\text{BiTeI}$  are on the order of 100 nm [23] and maybe small enough to result in a mixed work function when measured by the secondary electron cutoff technique. The corresponding work function of 5.2 eV is given in parentheses in Table I and lies in between the values found for Te- and I-terminated surface areas by STM [22].

## B. Surface electronic structure

Figure 3 shows ARPES data obtained for  $\text{BiTeBr}$  and  $\text{BiTeCl}(0001)$  surfaces. The band structures vary greatly between Te- and Br/Cl-terminated surfaces, but, for a given termination, are similar for both materials. This is in agreement with previous results [8]. On the Te-terminated surface we observe a Rashba-split band close to the Fermi level that derives from the conduction band bottom and the onset of valence band states at a binding energy of approximately 1 eV. We note that only one set of parabolic bands is visible in our data whereas previous studies observed two to three sets of bands [7,25]. In Refs. [7,25] the lowest detected bands have their minima below  $-0.4$  eV while in our case at roughly  $-0.2$  eV. This could point to a different n-type doping at the surface or in the bulk. Another possible explanation is strong cross section effects with excitation energy which were reported recently [25]. For the Br/Cl-terminated surface, conduction band states do not appear at the Fermi level due to p-type band bending as well as no surface states emerge near the valence band in agreement with earlier ARPES measurements on  $\text{BiTeCl}$  and in contradiction with a theoretical prediction [6]. The onset of spectral weight derived from the valence band lies at binding energies of approximately 0.7–0.8 eV.

The electronic structure determined by ARPES is in fair agreement with the  $dI/dV$  maps in Fig. 1, concerning, e.g., the presence or absence of surface states at the Fermi level depending on termination. In accordance with previous findings for  $\text{BiTeI}$  we observe significant time-dependent shifts to higher binding energies in the electronic structure of the  $X$ -terminated surfaces while those are much reduced for the Te termination [23]. This can be attributed to residual gas absorption that is enhanced for the  $X$  terminations, as already suggested by our STM data. More rapid energy shifts were observed during operation of the He lamp, possibly as a result of hydrogen adsorption, which might explain the discrepancy between the valence band offsets determined by ARPES (Fig. 3) and by the  $dI/dV$  maps in Fig. 1 as well as the absence of the surface states on the  $X$  terminations.

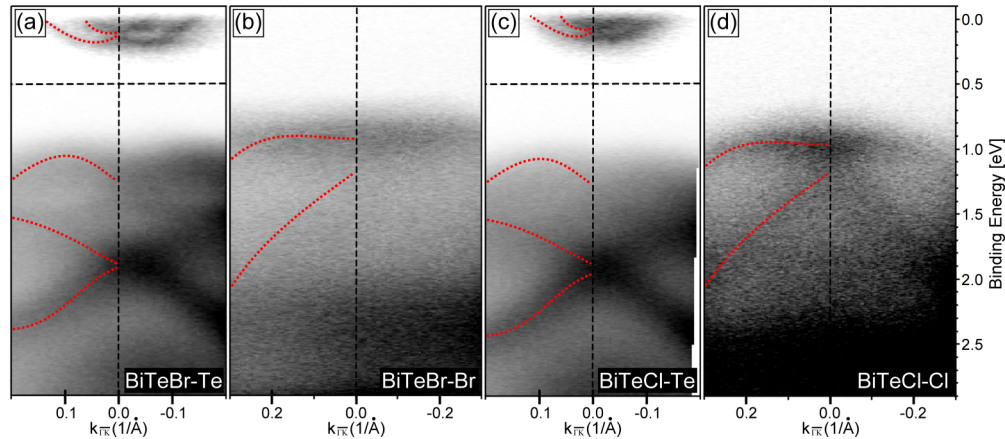


FIG. 3. (Color online) Angle-resolved photoemission data for BiTeBr in (a) and (b), and for BiTeCl in (c) and (d) ( $h\nu = 21.2$  eV). The contrast between  $E_F$  and 0.5 eV (indicated by horizontal lines) has been increased in (a) and (c) for better visibility of the Rashba-split band near  $E_F$ . The red dotted lines serve as guides to the eye.

Similarly to the XPS spectra in Fig. 2 also the ARPES data in Fig. 3 reflect the complete surface area of our samples because the spot sizes of the light sources exceed the lateral sample dimensions. The results therefore confirm the single termination of BiTeBr and BiTeCl on a macroscopic scale, in line with the STM data in Fig. 1. This excludes any considerable appearance of different crystal phases. The measured band structures show no topological surface state that would bridge the gap between valence and conduction bands, excluding a possible topological insulator phase in BiTeCl [24,26].

Since the electronic structure of BiTeX near the surface is highly termination-dependent it is of interest to investigate additional possibilities to modify the surface electronic properties. Figure 4 summarizes the influence of Cs adsorption on the surfaces of BiTeCl. Surprisingly, we observe energy shifts in the spectra into opposite directions for the two terminations: While for the Cl-terminated surface the features shift to higher binding energy—as expected for adsorption of alkali species [4,23,44]—they shift to lower binding energy for the Te-terminated surface. This trend is observed in the valence band [see Figs. 4(b) and 4(e)] and in the core levels [see Figs. 4(a) and 4(d)]. The positive energy shift on the Te-terminated surface is rather unusual and may occur in the present case due to clustering of the Cs adsorbates, as observed by STM in Fig. 4(f). In Ref. [23] we showed for BiTeI that the diffusion length of Cs atoms at room temperature is considerably higher for Te- than for I-terminated surfaces [23], which could explain the strong clustering observed in Fig. 4(f). For the Cl-termination the appearance of the Cs-induced structures in STM is different and reveals flatter areas with reduced  $dI/dV$  signal [see Fig. 4(c)]. As seen in Fig. 4(b) the conduction band minimum shows up below the Fermi level upon Cs deposition on the Cl-terminated surface, indicating that it is located slightly above the Fermi level for the pristine surface. In summary, the results indicate that the surface termination can considerably affect the adsorption behavior of adatoms and the resulting influence on the electronic structure, which might be of relevance, e.g., for interfacing BiTeX with other materials. Similar effects to those presented here for

Cs/BiTeCl were also observed for Cs/BiTeBr (not shown), namely an energy shift to higher binding energies on the Br termination and a clustering of Cs on the Te termination in combination with an energy shift to lower binding energies.

### C. Atomic defects

After identifying the surface termination, we reglued the samples with a top post and moved them to a separate LT-STM, operated at  $T = 5$  K, to cleave them again. Figure 5 shows data obtained at a positive gap voltage, usually resulting in increased (decreased) contrast for defects that act as electron donors (acceptors) [45].

If we assume that the sample only consists of three elements, for example Bi, Te, and Br, three kinds of defects may appear, e.g., in the Br layer: a vacancy, a Te antisite, and a Bi antisite. We expect that the electronegativity behaves as  $\text{Bi} < \text{Te} < \text{Br}$  (as shown in our DFT calculations) and that charge of two neighboring atoms is transferred from the one with lower to the one with higher electronegativity. The atomic radii behave as  $\text{Bi} > \text{Te} > \text{Br}$ . One can assume that it is more likely for a vacancy to be substituted by a smaller atom than forming an antisite with a larger atom.

In another publication we showed a  $400 \text{ nm}^2$  scan of the Te termination of BiTeI [23] which revealed defect densities of roughly  $7.5/(100 \text{ nm}^2)$  in the third layer (I) and  $2.5/(100 \text{ nm}^2)$  in the first layer (Te). Figure 5(a) shows the Te termination of BiTeBr (scan area  $75 \text{ nm} \times 75 \text{ nm}$ ) measured at 1 V gap voltage and 10 pA tunneling current. With the same method [45], we can identify defect densities of about  $2.5/(100 \text{ nm}^2)$  in the third layer (Br) and  $1.3/(100 \text{ nm}^2)$  in the first layer (Te). No defects in the second layer (Bi) have been found.

Adsorbates, marked by a black arrow, appear to be around 2.5 nm high and vary in shape, while defects labeled A are only 25 pm high and 1 nm in diameter. They show an increased contrast and in the zoom-in in Fig. 5(b) one further recognizes that the atoms around the defect center appear darker. This is an indication of a local charge transfer from the surrounding to

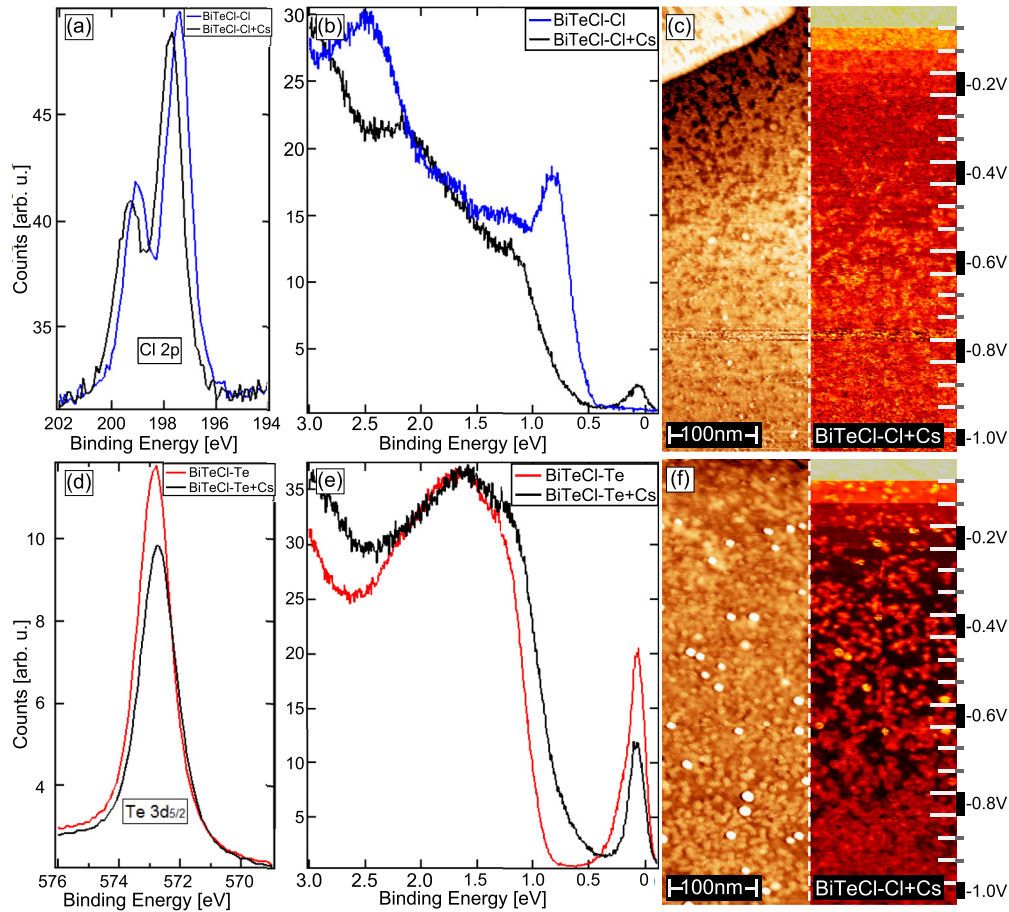


FIG. 4. (Color online) Effect of Cs adsorption on BiTeCl(0001). Panels (a) and (d) show core level spectra measured before and after Cs deposition on a Te- and a Cl-terminated surface, respectively. Corresponding valence band spectra taken at the  $\bar{\Gamma}$  point are shown in (b) and (e) ( $h\nu = 21.2$  eV). STM images and  $dI/dV$  maps acquired after deposition of Cs on Te- and Cl-terminated BiTeCl are given in (c) and (f).

the defect atom. Defect B shows a reduced DOS indicating a charge transfer from the defect to the surrounding. Comparing the defects A and B by means of total numbers and relative contrast, we conclude that A is a Br antisite while B is most likely a Bi antisite or a vacancy.

Now we analyze the three different third-layer defects by means of total number and relative contrast. Defect C appears most often and features the highest contrast. Since the third layer of the Te termination of BiTeBr is Br, having the smallest atomic radius and largest electronegativity, a Br vacancy could be a reasonable candidate. Furthermore, the basic structure of defect D is the same defect as C with an additional atom on top. A possible explanation is a Br atom which remains on the surface after the cleaving process. Defect E appears less often than C but more often than defect F and has the lowest contrast. The atomic radius of Br is closer to Te than to Bi, which would lead to a Te antisite in the Br layer. Also the fact that the contrast is weak could be due to the smaller difference in electronegativity of Te and Br compared to Bi. F is the defect that appears most rarely, which may indicate a Bi antisite in the Br layer. The high contrast contradicts these assumptions, but a closer comparison between C and F shows an inversion of the contrast. While the center of defect C shows a higher DOS than the direct surrounding, for F the situation is opposite: a low intensity in the center with a bright surrounding. If we expect

a Bi antisite in the Br layer, the Bi would donate an electron, which would result in a higher DOS at the location of the defect [45]. Also the center of defect E shows a dark contrast with a brighter surrounding which would be in line with our assumptions, since both Bi and Te are less electronegative compared to Br, so they would act as electron donors.

Figures 4(e) and 4(f) provide side- and top-view sketches of particular atomic defects in the second and third atomic layer, respectively. While a defect in a certain layer affects nearest-neighbor (NN) atoms, the resulting pattern on the surface gets more extended the deeper the defect is located. A second-layer defect (2nd) would result in a contrast change of three NN atoms on the surface. A third-layer defect (3rd) results in a contrast change of three next-nearest-neighbor surface atoms, as can be seen in Fig. 4(b), defect C. Defects such as E and F appear when the third-layer defect (Br) influences the NN (Bi; 2nd layer) differently, e.g., acting as an electron donor instead of an electron acceptor. The result is a Bi atom acting like a second-layer defect and therefore in three Bi atoms influencing three neighboring atoms (Te) each.

Like on BiTeI [23] no defects below the third layer could be found, possibly due to the van der Waals gap. The whole surface seems to be corrugated, as can be seen on the bottom part of Fig. 5(a) at the dark and bright area, which might be the result of screw dislocations. If we compare the Te termination

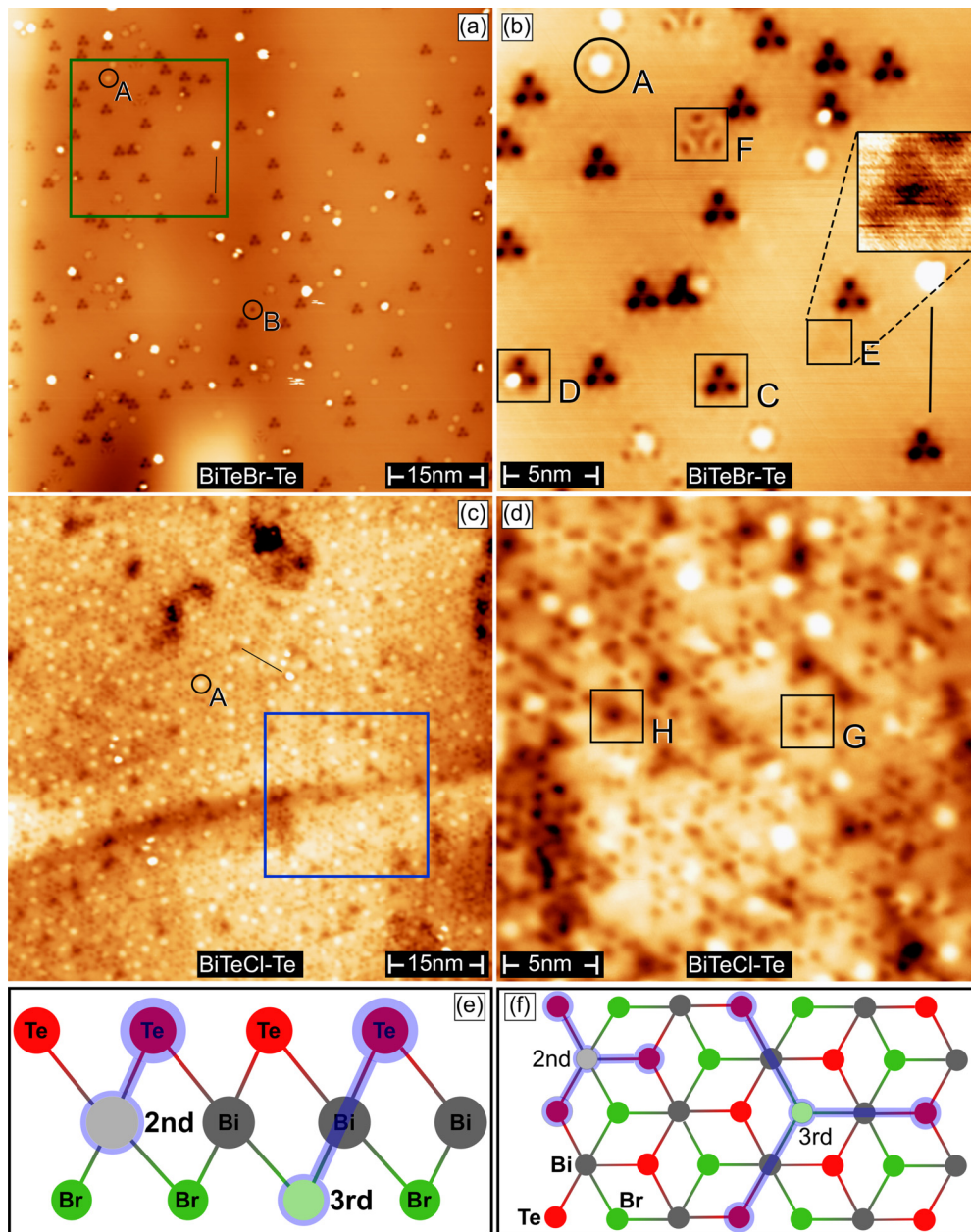


FIG. 5. (Color online) LT-STM measurements; all scans are performed at  $T = 5$  K,  $V = 1$  V, and  $I = 10$  pA. (a) The Te termination of BiTeBr shows the lowest defect density of the BiTeX family. Panel (b) is the zoom-in of (a) at the green square. We can find mainly one type of surface defect and three different types of third-layer defects with an additional variation, but no second-layer defects could be found. Panel (c) shows the Te termination of BiTeCl. The defect density is the highest of the BiTeX compounds. Panel (d) shows the zoom-in of (c). One can find at least two different types of defects; others might be covered. (e) Side view of a hard ball sketch of BiTeBr-Te. Second (2nd) and third (3rd) layer defects and their effect on nearest-neighbor atoms are indicated schematically. (f) Top view of a hard ball sketch of BiTeBr-Te. Second-layer defects would result in three neighboring Te atoms with different contrast while third-layer defects mainly affect three next-nearest-neighbor Te atoms, as can be seen in defect C in panel (b).

of BiTeBr and BiTeI, the defects E and F of Fig. 5(a) are very similar to the defects E and F from Fig. 2 in Ref. [23], which could also be Te and Bi antisites.

The defect density in BiTeCl [Fig. 5(c)] is much higher as compared to BiTeBr. It is difficult to find a vacancy in the first layer but adsorbates (black arrow) and antisites (A) can frequently be found. Figure 5(d) is the magnified view of the blue-framed square shown in Fig. 5(c). It is hard to point out certain defects but (G) and (H) probably represent different

third-layer defects, most likely a vacancy and a Te antisite, respectively.

So far measurements in the LT-STM were only successful for the Te-terminated surfaces of BiTeBr and BiTeCl. However, third-layer defects of Te should be equal to first-layer defects of X, as long as they are not induced by the cleaving process. This would mean at least for BiTeBr that the Bi layer is almost free of defects and that the Te layer has fewer defects than the Br layer.



#### IV. DISCUSSION

Comparing the three BiTeX compounds the most obvious difference is the presence ( $X = \text{I}$ ) or absence ( $X = \text{Cl, Br}$ ) of stacking faults in the bulk crystal structure resulting in surfaces with mixed or single terminations, respectively. On the atomic scale, however, BiTeCl stands out with a considerably larger defect density than the two other compounds. Hence, in this respect BiTeBr currently appears to be the material with the most homogeneous structural properties. This finding nicely complements comparative studies of the surface electronic properties of BiTeX that suggests BiTeBr as the best candidate for possible future applications [8,19].

We further note that a possible migration of Bi atoms into the topmost Te layer was speculated to occur in all three BiTeX compounds based on the observation of a second component in the Bi  $5d$  core level signal for Te-terminated surfaces [8]. In our STM measurements for BiTeBr, however, such defects involving the first (Te) and the second (Bi) layer are not found. On the other hand, also no additional component in the Bi core level spectra is observed in the present study, in agreement with a previous report on BiTeCl [6].

The role of structural defects is furthermore important for a basic understanding of the electronic properties in BiTeX. For BiTeCl a lift-off during the cleaving process of a thin freestanding layer (around 1 unit cell) that remains loosely on the crystal surface has been proposed to give rise to the Rashba-split surface bands observed in ARPES and to mask the presence of a topological state on the intrinsic surface [26]. This scenario is not supported by the present combined STM and ARPES results that show step edge heights of the surface terraces matching the bulk unit cell and, at the same time, provide no indication of topological surface bands. It is furthermore worth noting that, while the atomic defect density observed here in STM is considerably higher for BiTeCl than for BiTeBr, the quality of the ARPES data turns out to be comparable and also the measured band structures are very similar. This observation is in contrast to a recent investigation of BiTeCl that concluded qualitative changes in the electronic structure depending on the amount of defects near the surface [24].

The broken inversion symmetry in BiTeX in combination with the high electronegativity of the halogen atoms is assumed to induce a net dipole moment in the bulk unit cell [22,26] that, in turn, gives rise to n- or p-type band bending at the surface depending on termination [4]. The proposed microscopic

picture of the charge distribution is often based on a covalently bound  $(\text{BiTe})^+$  bilayer that couples ionically to the adjacent  $X^-$  layer [4,8,20,39]. However, the bonding character has also been viewed as ionic for both Bi-Te and Bi-X based on the fact that the valence (conduction) band is to a great extent Te/ $X$  (Bi) derived, which indicates significant charge transfer from Bi to Te and  $X$  [46]. In some calculations even a larger charge transfer to Te than to  $X$  has been obtained [26,47]. Direct experimental information on this issue has so far been scarce. The present XPS measurements indeed point to a substantial charge donation from Bi to Te and  $X$  which is in line with our first-principles calculations of the local atomic charges. On the other hand, the large work function differences between Te- and  $X$ -terminated surfaces confirm the presence of a dipole moment in the unit cell and, thus, support the view of a  $(\text{BiTe})^+$  block with positive net charge that forms a polar bond with the  $X^-$  layer.

#### V. SUMMARY

We have presented a comparative study of the structural and electronic surface properties of the noncentrosymmetric giant-Rashba semiconductors BiTeX(0001) ( $X = \text{Cl, Br, I}$ ). Cleaving of single-crystalline samples exposes macroscopically homogeneous surfaces with Te- and  $X$ -termination for BiTeCl and BiTeBr, in contrast to BiTeI where bulk stacking faults are known to give rise to mixed surface terminations. STM and XPS data confirm the unit cell heights and atomic stacking orders that are expected from the bulk crystal structure. The electronic band structures measured by ARPES differ considerably depending on surface termination, but in no case topological surface states are observed. The chemical bonding in BiTeX is found to be characterized by substantial charge transfer from Bi to Te and  $X$ . However, based on work function measurements we also obtain evidence for ionic bonding between  $(\text{BiTe})^+$  bilayers and  $X^-$  layers, whereas the polarity of the bond increases with rising electronegativity of the halogen atom.

#### ACKNOWLEDGMENTS

This work was financially supported by the Deutsche Forschungsgemeinschaft through FOR1162 and partly by the Ministry of Education and Science of Russian Federation (Grant No. 2.8575.2013), the Russian Foundation for Basic Research (Grants No. 15-02-01797 and No. 15-02-02717), and Saint Petersburg State University (Project No. 11.50.202.2015).

---

[1] K. Ishizaka, M. S. Bahramy, H. Murakawa, M. Sakano, T. Shimojima, T. Sonobe, K. Koizumi, S. Shin, H. Miyahara, A. Kimura, K. Miyamoto, T. Okuda, H. Namatame, M. Taniguchi, R. Arita, N. Nagaosa, K. Kobayashi, Y. Murakami, R. Kumai, Y. Kaneko, Y. Onose, and Y. Tokura, *Nat. Mater.* **10**, 521 (2011).  
 [2] S. V. Eremeev, I. A. Nechaev, Yu. M. Koroteev, P. M. Echenique, and E. V. Chulkov, *Phys. Rev. Lett.* **108**, 246802 (2012).

[3] H. Murakawa, M. S. Bahramy, M. Tokunaga, Y. Kohama, C. Bell, Y. Kaneko, N. Nagaosa, H. Y. Hwang, and Y. Tokura, *Science* **342**, 1490 (2013).  
 [4] A. Crepaldi, L. Moreschini, G. Autès, C. Tournier-Colletta, S. Moser, N. Virk, H. Berger, Ph. Bugnon, Y. J. Chang, K. Kern, A. Bostwick, E. Rotenberg, O. V. Yazyev, and M. Grioni, *Phys. Rev. Lett.* **109**, 096803 (2012).  
 [5] G. Landolt, S. V. Eremeev, Y. M. Koroteev, B. Slomski, S. Muff, T. Neupert, M. Kobayashi, V. N. Strocov, T. Schmitt, Z.

- S. Aliev, M. B. Babanly, I. R. Amiraslanov, E. V. Chulkov, J. Osterwalder, and J. H. Dil, *Phys. Rev. Lett.* **109**, 116403 (2012).
- [6] G. Landolt, S. V. Ereemeev, O. E. Tereshchenko, S. Muff, B. Slomski, K. A. Kokh, M. Kobayashi, T. Schmitt, V. N. Strocov, J. Osterwalder, E. V. Chulkov, and J. H. Dil, *New J. Phys.* **15**, 085022 (2013).
- [7] M. Sakano, M. S. Bahramy, A. Katayama, T. Shimojima, H. Murakawa, Y. Kaneko, W. Malaeb, S. Shin, K. Ono, H. Kumigashira, R. Arita, N. Nagaosa, H. Y. Hwang, Y. Tokura, and K. Ishizaka, *Phys. Rev. Lett.* **110**, 107204 (2013).
- [8] L. Moreschini, G. Autès, A. Crepaldi, S. Moser, J. C. Johannsen, K. S. Kim, H. Berger, Ph. Bugnon, A. Magrez, J. Denlinger, E. Rotenberg, A. Bostwick, O. V. Yazyev, and M. Grioni, *J. Electron Spectrosc. Relat. Phenom.* **201**, 115 (2015).
- [9] C. Martin, E. D. Mun, H. Berger, V. S. Zapf, and D. B. Tanner, *Phys. Rev. B* **87**, 041104(R) (2013).
- [10] C. Bell, M. S. Bahramy, H. Murakawa, J. G. Checkelsky, R. Arita, Y. Kaneko, Y. Onose, M. Tokunaga, Y. Kohama, N. Nagaosa, Y. Tokura, and H. Y. Hwang, *Phys. Rev. B* **87**, 081109(R) (2013).
- [11] M. S. Bahramy, R. Arita, and N. Nagaosa, *Phys. Rev. B* **84**, 041202(R) (2011).
- [12] M. S. Bahramy, B.-J. Yang, R. Arita, and N. Nagaosa, *Nat. Commun.* **3**, 679 (2011).
- [13] S. Datta and B. Das, *Appl. Phys. Lett.* **56**, 665 (1990).
- [14] I. Žutić, J. Fabian, and S. Das Sarma, *Rev. Mod. Phys.* **76**, 323 (2004).
- [15] C. R. Ast, J. Henk, A. Ernst, L. Moreschini, M. C. Falub, D. Pacilé, P. Bruno, K. Kern, and M. Grioni, *Phys. Rev. Lett.* **98**, 186807 (2007).
- [16] H. Bentmann and F. Reinert, *New J. Phys.* **15**, 115011 (2013).
- [17] L. El-Kareh, P. Sessi, T. Bathon, and M. Bode, *Phys. Rev. Lett.* **110**, 176803 (2013).
- [18] L. El-Kareh, G. Bihlmayer, A. Buchter, H. Bentmann, S. Blügel, F. Reinert, and M. Bode, *New J. Phys.* **16**, 045017 (2014).
- [19] S. V. Ereemeev, I. P. Rusinov, I. A. Nechaev, and E. V. Chulkov, *New J. Phys.* **15**, 075015 (2013).
- [20] C. J. Butler, H.-H. Yang, J.-Y. Hong, S.-H. Hsu, R. Sankar, C.-I. Lu, H.-Y. Lu, K.-H. O. Yang, H.-W. Shiu, C.-H. Chen, C.-C. Kaun, G.-J. Shu, F.-C. Chou, and M.-T. Lin, *Nat. Commun.* **5**, 4066 (2014).
- [21] C. Tournier-Colletta, G. Autès, B. Kierren, Ph. Bugnon, H. Berger, Y. Fagot-Revurat, O. V. Yazyev, M. Grioni, and D. Malterre, *Phys. Rev. B* **89**, 085402 (2014).
- [22] Y. Kohsaka, M. Kanou, H. Takagi, T. Hanaguri, and T. Sasagawa, *Phys. Rev. B* **91**, 245312 (2015).
- [23] S. Fiedler, L. El-Kareh, S. V. Ereemeev, O. E. Tereshchenko, C. Seibel, P. Lutz, K. A. Kokh, E. V. Chulkov, T. V. Kuznetsova, V. I. Grebennikov, H. Bentmann, M. Bode, and F. Reinert, *New J. Phys.* **16**, 075013 (2014).
- [24] Y. J. Yan, M. Q. Ren, X. Liu, Z. C. Huang, J. Jiang, Q. Fan, J. Miao, B. P. Xie, F. Xiang, X. Wang, T. Zhang, and D. L. Feng, *J. Phys.: Condens. Matter* **27**, 475004 (2015).
- [25] A. Crepaldi, F. Cilento, M. Zacchigna, M. Zonno, J. C. Johannsen, C. Tournier-Colletta, L. Moreschini, I. Vobornik, F. Bondino, E. Magnano, H. Berger, A. Magrez, Ph. Bugnon, G. Autès, O. V. Yazyev, M. Grioni, and F. Parmigiani, *Phys. Rev. B* **89**, 125408 (2014).
- [26] Y. L. Chen, M. Kanou, Z. K. Liu, H. J. Zhang, J. A. Sobota, D. Leuenberger, S. K. Mo, B. Zhou, S.-L. Yang, P. S. Kirchmann, D. H. Lu, R. G. Moore, Z. Hussain, Z. X. Shen, X. L. Qi, and T. Sasagawa, *Nat. Phys.* **9**, 704 (2013).
- [27] I. Horcas, R. Fernández, J. M. Gómez-Rodríguez, J. Colchero, J. Gómez-Herrero, and A. M. Baro, *Rev. Sci. Instrum.* **78**, 013705 (2007).
- [28] S. Trasatti, *J. Electroanal. Chem. Interfacial Electrochem.* **54**, 19 (1974).
- [29] P. C. Rusu and G. Brocks, *Phys. Rev. B* **74**, 073414 (2006).
- [30] A. Tomokiyo, T. Okada, and S. Kawano, *Jpn. J. Appl. Phys.* **16**, 291 (1977).
- [31] U. Petasch, C. Hennig, and H. Oppermann, *Z. Naturforsch.* **54b**, 234 (1999).
- [32] K. A. Kokh, S. V. Makarenko, V. Golyashov, O. A. Shegai, and O. E. Tereshchenko, *CrystEngComm* **16**, 581 (2014).
- [33] P. E. Blöchl, *Phys. Rev. B* **50**, 17953 (1994).
- [34] G. Kresse and D. Joubert, *Phys. Rev. B* **59**, 1758 (1999).
- [35] J. P. Perdew, K. Burke, and M. Ernzerhof, *Phys. Rev. Lett.* **77**, 3865 (1996).
- [36] G. Kresse and J. Hafner, *Phys. Rev. B* **48**, 13115 (1993).
- [37] G. Kresse and J. Furthmüller, *Comput. Mater. Sci.* **6**, 15 (1996).
- [38] W. Tang, E. Sanville, and G. Henkelman, *J. Phys.: Condens. Matter* **21**, 084204 (2009).
- [39] A. V. Shevelkov, E. V. Dikarev, R. V. Shapanchenko, and B. A. Popovkin, *J. Solid State Chem.* **114**, 379 (1995).
- [40] S. Hüfner, *Photoelectron Spectroscopy: Principles and Applications*, 3rd ed. (Springer Verlag, Berlin, Heidelberg, 2003).
- [41] R. B. Shalvoy, G. B. Fisher, and P. J. Stiles, *Phys. Rev. B* **15**, 1680 (1977).
- [42] M. V. Kuznetsov, L. V. Yashina, J. Sánchez-Barriga, I. I. Ogorodnikov, A. S. Vorokh, A. A. Volykhov, R. J. Koch, V. S. Neudachina, M. E. Tamm, A. P. Sirotnina, A. Yu. Varykhalov, G. Springholz, G. Bauer, J. D. Riley, and O. Rader, *Phys. Rev. B* **91**, 085402 (2015).
- [43] V. Wagner, G. Dolling, B. M. Powell, and G. Landwehr, *Phys. Status Solidi B* **85**, 311 (1978).
- [44] C. Seibel, H. Maaß, M. Ohtaka, S. Fiedler, C. Jünger, C.-H. Min, H. Bentmann, K. Sakamoto, and F. Reinert, *Phys. Rev. B* **86**, 161105(R) (2012).
- [45] Y. Jiang, Y. Y. Sun, M. Chen, Y. Wang, Z. Li, C. Song, K. He, L. Wang, X. Chen, Q.-K. Xue, X. Ma, and S. B. Zhang, *Phys. Rev. Lett.* **108**, 066809 (2012).
- [46] Z. Zhu, Y. Cheng, and U. Schwingenschlögl, *New J. Phys.* **15**, 023010 (2013).
- [47] Y. Ma, Y. Dai, W. Wei, X. Li, and B. Huang, *Phys. Chem. Chem. Phys.* **16**, 17603 (2014).